analytical chemistry

Article

Cite This: *Anal. Chem.* 2018, 90, 13572−13579

pubs.acs.org/ac

Design of Hydrogel Particle Morphology for Rapid Bioassays

Sarah J. Shapiro,[†] Dhananjaya Dendukuri,[‡] and Patrick S. Doyle*[,†]

[†]Department of Chemical Engineering, Massachusetts Institute of Technology, Cambridge, Massachusetts 02139, United States

[‡]Achira Laboratories Pvt. Ltd., 66B, 13th Cross Road, Dollar Layout, JP Nagar Phase III, Bangalore 560078, India

Supporting Information

ABSTRACT: Hydrogel microparticles have been extensively used in the field of medical diagnostics for detecting targets ranging from proteins to nucleic acids. However, little is known about how the shape of hydrogel particles impacts the signal from a bioassay. In this article, we analyze the flux into porous hydrogel particles to develop scaling laws for the signal from a point-of-care bioassay. The signal can be increased by increasing the ratio of the surface area of the hydrogel particle to the two-dimensional projected imaging area used for analysis. We show that adding internal surface area to hydrogel particles increases the assay signal in a biotin−streptavidin bioassay. We also demonstrate the application of this technique to a protein-based assay for thyroid-stimulating hormone, reducing the limit of detection of the assay sixfold by changing particle shape. We anticipate that these strategies can be used broadly to optimize hydrogel-based systems for point-of-care diagnostics.

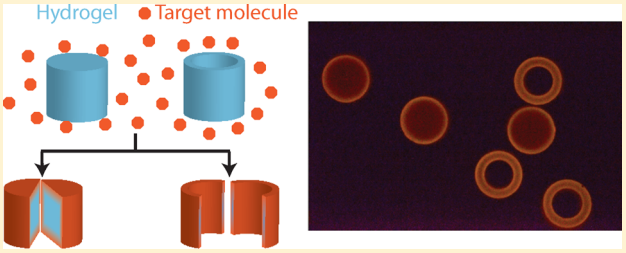

Hydrogel microparticles have found widespread applications in biosensing applications.[1] Although hydrogels are typically biologically inert and nonfouling in the presence of biological materials, they can be functionalized with reactive molecules to enable their use as capture or release agents for diagnostic or therapeutic applications. The wide variety of materials for hydrogels[2−4] and of methods of hydrogel functionalization[5−7] has ensured their versatility for a wide range of applications. These particles vary in size from a few to hundreds of micrometers[8] and the advent of technologies such as stop-flow lithography (SFL),[9] micromolding,[10] and 3D printing[11] enable facile control over hydrogel shape and size in addition to function.

The versatility of hydrogels has previously been utilized to develop point-of-care (POC) diagnostics[12−14] in an effort to make diagnostic tests more accessible. POC diagnostics enable diagnosis of disease wherever care is delivered to patients, including doctor's clinics, patient bedsides, and in patient's homes, facilitating more rapid treatment.[15] In contrast, sending samples to a centralized laboratory results in delays of at least 1−2 h in European countries, typically requiring non-emergency patients to receive their test results at a later time or date.[16] Incorporating POC testing was previously shown to reduce mean test turnaround time from 59 to 8 min.[17] In developing countries, POC testing has the potential to increase test accessibility more drastically, as only an estimated 28% of the population in Africa has access to advanced health care facilities.[18] Implementing POC testing is particularly important in regions where centralized laboratories are less prevalent or in acute conditions where time to diagnosis is critical.[19,20]

Protein-based assays are extremely important in diagnostics, with more than 200 different protein targets from serum or plasma analyzed in clinical laboratories, an estimated 10% of all proteins known to exist in plasma.[21,22] Among immunoassays, tests for thyroid function are widely utilized, as thyroid diseases affect around 200 million people worldwide.[23] Because of the function of thyroid-stimulating hormone (TSH) in regulating thryroid hormone levels, it is used as a diagnostic marker either alone or in panels for a wide variety of thyroid disorders.[24,25] TSH is typically measured in central laboratories using large-scale analyzers.[26] In countries where centralized laboratories are less prevalent, this can lead to reduced test availability and a lack of diagnoses. In India, for example, an estimated 42 million people are suffering from thyroid disease, with more than 10% of the adult population suffering from hypothyroidism, around one third of whom are undiagnosed.[27−29]

Although hydrogels have been used extensively and there is a large body of literature on their formulation and applications, little is known about the influence of hydrogel shape on diagnostics. Previously, hydrogel shapes have been used as a method of enabling multiplexing,[30−32] for enhancing cell capture,[33] for increasing cellular uptake,[34] and for generating vasculature in tissue-engineering scaffolds.[35] Previous studies have also analyzed the time-dependent binding of target molecules in hydrogels for biosensing applications.[36,37] However, these studies assumed a specific shape profile for the hydrogel and did not explore variations. To our knowledge, no studies have analyzed the impact of hydrogel particle morphology on bioassay signal. Our study uses poly(ethylene glycol) microparticles to explore the influence of shape on the fluorescent signal for point-of-care bioassays.

Received: August 16, 2018
Accepted: October 19, 2018
Published: October 19, 2018

DOI: 10.1021/acs.analchem.8b03728
Anal. Chem. 2018, 90, 13572−13579

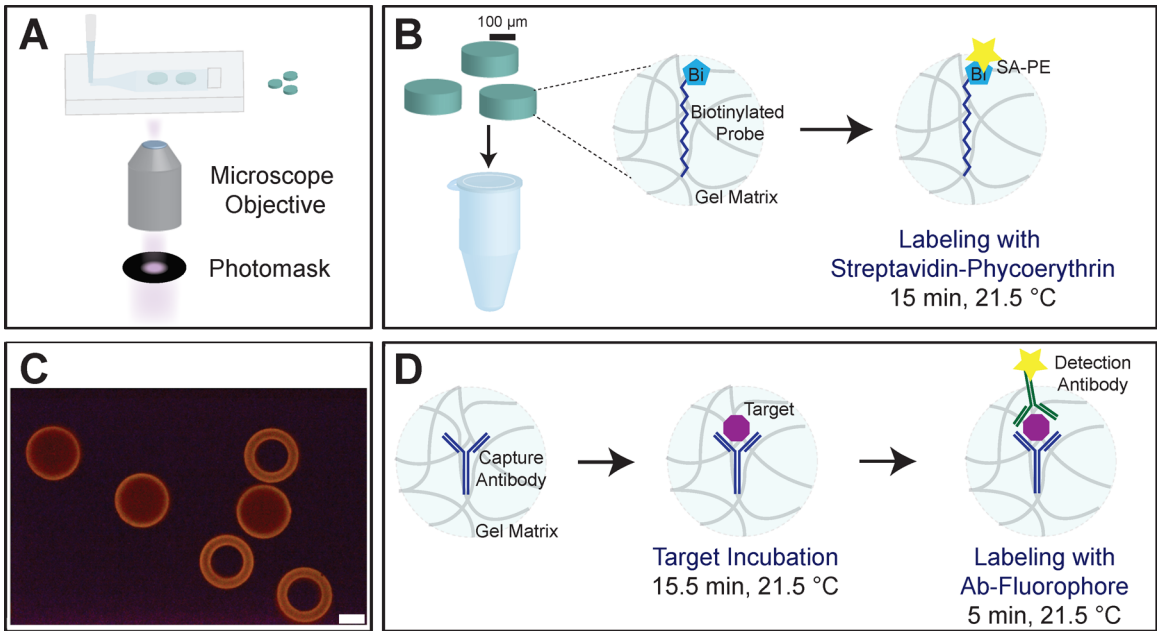

Figure 1. (A) Fabrication of hydrogel particles using projection lithography in a microfluidic channel. The particles were polymerized using UV light shining through a photomask placed in the field stop of the microscope. (B) Labeling assay with streptavidin−phycoerythrin. A DNA probe with a biotin molecule was covalently incorporated into the hydrogel particles during polymerization. The biotin reacted with streptavidin−phycoerythrin (SAPE) during a 15 min incubation at 21.5 °C. (C) Fluorescent image of disk particles and ring particles with 60 μm inner radius showing particle uniformity after reaction with SAPE. Scale bar is 100 μm. (D) Sandwich assay protocol for antibody assay for protein detection. Capture antibody was immobilized within the hydrogel during polymerization. The gels were then incubated with the target antigen for 15.5 min at 21.5 °C. After washing, the particles were labeled by incubation with a fluorophore-conjugated detection antibody for 5 min at 21.5 °C.

We explored methods of improving the limit of detection of point-of-care bioassays through manipulating the hydrogel shape. We observed that often, although the three-dimensional (3D) hydrogels are porous to enable target capture, because of the relative rates of reaction and diffusion, only the edges of the hydrogel are utilized for binding.[36,38] We determined that to maximize the fluorescent signal, it is optimal to maximize both diffusion and reaction rates while decreasing the cross-sectional area of the hydrogel parallel to the imaging plane to concentrate the signal in a small area. By calculating the flux of target into the hydrogel, we were able to obtain estimates of the final signal per unit imaging area at the end of the bioassay. To validate our theory, we performed experiments wherein we used projection lithography to form hydrogel microparticles with varying surface area and analyzed the resulting signal in the hydrogel microparticles after labeling a biotin probe with a fluorescent streptavidin molecule. By using ring structures instead of disk shapes, we were able to add additional surface area on the inside of the microparticle, thereby increasing signal in the bioassay. Finally, we applied the method to reduce the limit of detection in a protein-based assay for TSH by a factor of 6. In this study, we achieve a limit of detection of 0.056 μIU/mL, below the 0.1 μIU/mL threshold that distinguishes between grade 1 and grade 2 hyperthyroidism,[39] with a short 15.5 min target incubation, surpassing second-generation TSH tests.[40]

EXPERIMENTAL SECTION

Particle Synthesis. Hydrogel particles were synthesized using a variation of stop-flow lithography (SFL).[6,9] The precursor solution was formed from a stock monomer solution consisting of 20% polyethylene glycol diacrylate (PEG-DA) 700, 40% polyethylene glycol 200, 5% Darocur 1173 photoinitiator (all from Sigma-Aldrich), and 35% buffer. For studies with biotinylated probe, 3× Tris-EDTA buffer (30 mM Tris, 3 mM EDTA) was used (EMD Millipore), while for antibody incorporation 1× phosphate buffered saline (PBS) buffer was used (Corning). The stock monomer solution was diluted 9:1 with probe or antibody solution. The biotinylated probe consisted of a DNA strand (sequence: 5′ ATA GCA GAT CAG CAG CCA GA 3′) with an Acrydite modification on the 5′ end and a biotin group on the 3′ end (Integrated DNA Technologies). This probe was used in concentrations of 10, 5, 0.5, or 0.05 μM in the prepolymer solution. For antibody-functionalized particles, anti-TSH 10-T25C antibody was purchased from Fitzgerald (Acton, MA) and conjugated to an acrylate group as described below for covalent incorporation into the hydrogels. The antibody was used at 0.4 mg/mL in the monomer solution. The final monomer solution was vortexed for 30 s before addition to a microfluidic chamber.

Microfluidic channels 150 μm tall and 450 μm wide were constructed of polydimethylsiloxane (PDMS). PDMS was mixed in a 10:1 ratio of base to curing agent and poured over a silicon wafer mold created from SU-8 photoresist. The mixture was allowed to rest for 45 min to remove bubbles and then placed in a 65 °C oven overnight. To construct microfluidic channels, a small drop of PDMS was sheared between two glass coverslips to create a thin layer. The coverslips were then partially cured for 18 min at 65 °C and then removed from the oven, and a PDMS channel from the silicon wafer mold was placed on top of the slide. The curing process was completed overnight at 65 °C.

Hydrogel particles were formed through a variant of SFL[6,9] on a Zeiss Axio Observer microscope as shown in Figure 1A. A mylar mask (Fineline Imaging) was placed in the field stop of the microscope and UV light from a UV LED (M365L2-C4,

DOI: 10.1021/acs.analchem.8b03728
Anal. Chem. 2018, 90, 13572−13579

ThorLabs) illuminated the monomer mixture for 100 ms in the microfluidic channel through a UV filter set (11000v2, Chroma Technology) using a 20× objective. To maximize the number of particles per batch of antibody, after polymerization, rather than flushing the channel with fluid, the channel was moved to a different region to enable the formation of additional particles. The particles were subsequently flushed from the channel and washed five times. For biotinylated particles, the particles were washed and resuspended in 1× Tris-EDTA buffer with 0.05% Tween-20 (1× TET buffer) and for antibody-functionalized particles, the particles were washed and resuspended in PBS with 0.1% Tween-20 (PBST buffer).

Antibody Functionalization. Capture antibodies from Fitzgerald (Acton, MA) were washed three times in PBS using centrifugal filters from EMD Millipore. The antibody concentration was measured using a NanoDrop 2000 spectrophotometer (Thermo Scientific) and adjusted to 7.14 mg/mL in the final reaction mixture, which also contained 1.67 mM NHS-PEG-Acrylate (Creative PEGworks) in PBS. After a 1 h incubation at room temperature on a tube rotator (MX-RD-E, SCILOGEX), Tris-HCl solution was added from a 100 mM stock to bring the final concentration to 16.6 mM to quench the reaction. After the reaction was quenched for 30 min at room temperature on the rotating mixer, the antibody was washed four times in PBS for 5 min at 14 000*g*. The final antibody concentration was adjusted to 10 mg/mL in PBS.

Hydrogel Optimization. For initial Damköhler number and shape studies, a simplified system using the reaction of streptavidin−phycoerythrin (SAPE) with biotinylated particles was utilized, as described in Figure 1B. Particles were added to an Eppendorf tube and the buffer was removed down to 5 μL. Then 50 μL of 50 μg/L SAPE was added to each tube. SAPE was purchased from Life Technologies and diluted in 1× TET buffer. The Eppendorf tubes were incubated on a thermoshaker (MultiTherm Shaker, Thomas Scientific) at 21.5 °C for 15 min, then washed three times with 500 μL 1× TET buffer by vortexing followed by a 2 min centrifugation step. The particles were then placed on a glass coverslip and imaged through a 20× objective on a Zeiss Axio Observer A1 microscope using a broad spectrum LED (X-CITE 120LED, Excelitas Technologies) as a fluorescence source and a XF101-2 filter set from Omega Optical. Images were acquired using Andor SOLIS software and an Andor Clara CCD camera. In most cases, five particles were analyzed for each condition, except when fewer particles were found after the bioassay, in which case fewer particles were analyzed. In all cases, at least three particles were analyzed for each data point. After imaging, the images were cropped with ImageJ (National Institutes of Health)[41] and the fluorescent signal was analyzed using custom Matlab scripts. A fluorescent image of particles after a bioassay is shown in Figure 1C.

Detection of Thyroid-Stimulating Hormone. For detection of thyroid-stimulating hormone (TSH), ∼10 particles per assay condition were added to an Eppendorf tube. The assay protocol is illustrated in Figure 1D. After removal of the buffer down to 5 μL, 50 μL of TSH standard (from Monobind TSH Accubind ELISA kit) were added. PBS was used as a negative control. Tween-20 (10%, 0.5 μL) was then added to prevent particles from sticking together or to the edges of the tube. The particles were incubated with the TSH target for 15.5 min on a thermoshaker (MultiTherm Shaker, Thomas Scientific) at 1500 rpm and 21.5 °C. Immediately after the target incubation, 500 μL of PBST was added and the particles were centrifuged for 2 min. After removal of the supernatant, the particles were washed two times by addition of 500 μL of PBST, vortexing for 2 min, and centrifugation for 2 min. It was observed that longer vortexing periods could reduce the fluorescent accumulation in the negative sample (data not shown), but to minimize assay time, a 2 min vortexing step was used.

After rinsing, the supernatant was removed down to 5 μL, and 50 μL of detection antibody was added at a final concentration of 10 μg/mL. The detection antibody was purchased from Biospacific (Anti-TSH 5409 SPTNE-5) and labeled with Dyomics DY647P4 NHS ester as described below. The particles were incubated with the labeling antibody for 5 min on the thermoshaker at 1500 rpm and 21.5 °C. After the incubation, 500 μL of PBST with 1% polyethylene glycol MW 400 (PBST−PEG) was added and the particles were centrifuged for 2 min. The particles were then rinsed three times in PBST−PEG and once in PBS before resuspension in PBST for imaging. The particles were then imaged as described previously, using a filter cube set from Semrock consisting of a FF660-Di01 filter (dichroic), a FF01-628/40 filter (exitation), and a FF01-692/40 filter (emission). The images were cropped and the wheel particle images were aligned in ImageJ and then analyzed with custom Matlab scripts.

The DY647P4 NHS ester was suspended in DMSO at 10 mg/mL for long-term storage at −20 °C. The antibody was buffer-exchanged into PBS using filter columns. After buffer exchange, the concentration was measured using a NanoDrop spectrophotometer and adjusted to 4 mg/mL using PBS. The conjugation reaction proceeded in a buffer containing 2.7 mg/mL antibody, 68.5 mM sodium bicarbonate in PBS, and 0.73 mg/mL DY647P4 NHS ester, with the remaining volume made up with PBS. The reaction proceeded for 1 h at room temperature on a tube rotator. After completion of the reaction, the antibody was washed six times in PBS using a filter column and the concentration was adjusted to 1.7 mg/mL using PBS.

RESULTS AND DISCUSSION

Analytical Modeling of Bioassay Signal. In this study we sought to optimize hydrogel performance for point-of-care bioassays by maximizing assay signal. Hydrogels have been used extensively for bioassay applications because of their nonfouling nature and the ability to covalently incorporate biomolecules for sensing applications.[1,42] For point-of-care (POC) diagnostics, the timing of the assay becomes critical and slow kinetics cannot be circumvented by long incubation times. For this reason, detailed understanding and optimization of the hydrogel is crucial for POC applications. During a hydrogel-based bioassay, target molecules diffuse into the hydrogel and react with immobilized probe molecules, resulting in a reaction-diffusion process. Previously, reaction-diffusion mechanisms in hydrogels have been studied for long time scale incubations for both protein and nucleic acid assays.[36,37] For the case of POC diagnostics, the key consideration is maximizing the signal obtained from short target incubation times, as FDA-approved POC technologies take from 30 s to 1 h.[43] Typically, these assays operate in a regime where the target concentration in solution is not significantly reduced over the assay time scales (calculations in Supporting Information).

We can estimate the signal from a bioassay by considering a hydrogel particle in a well-mixed tube. The goal of any POC

DOI: 10.1021/acs.analchem.8b03728
Anal. Chem. 2018, 90, 13572−13579

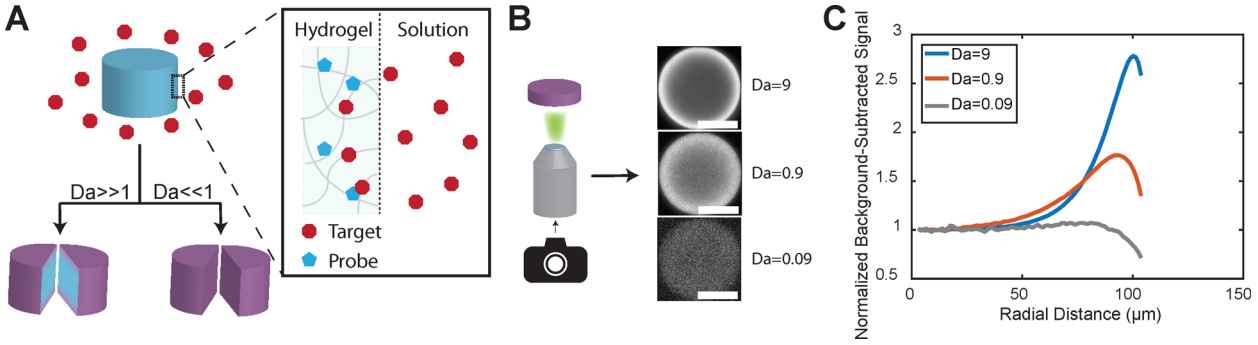

Figure 2. Signal variation within the hydrogel is dependent on the Damköhler number (*Da*). (A) Schematic representing reaction of target with immobilized probe within particle. At high Damköhler number (*Da*), the signal is localized around the edges of the hydrogel, while at low *Da* the signal is nearly uniform throughout the gel. (B) Imaging of 3D hydrogels, resulting in a 2D projection of the 3D signal profile. The images show actual biotinylated particles at various *Da*, thresholded to different values to illustrate the boundary layer profile. Scale bar is 100 μm. (C) Signal profile of biotinylated hydrogels at various *Da* after reaction with streptavidin−phycoerythrin for 15 min. The graph shows the radially averaged signal in the hydrogels, normalized to the center of the disk. Each trace is the average of five particles. *Da* was modified by changing the probe concentration in the hydrogels.

bioassay is to maximize the signal from the target captured within the hydrogel over the short assay time, which is related to the flux of target into the hydrogel, J. The flux can be described by Fick's law,[44] where D_{gel} is the diffusivity of the target in the hydrogel matrix and T is the target concentration:

$$J = -D_{gel}\nabla T \tag{1}$$

Many bioassays are performed under conditions where the rate of reaction within the hydrogel is much faster than the rate of diffusion.[36,38] The ratio of these rates is known as the Damköhler number (Da)[44] ($Da=\frac{k_a P_0 L^2}{D_{gel}}$). k_a represents the forward rate constant, P_0 the initial probe concentration, and L the distance from the center of the particle to the edge. Under conditions with high Da, where the reaction is much faster than diffusion, the target reacts with embedded probe before reaching the center of the hydrogel, and the binding is confined to a region around the edges of the hydrogel—the so-called boundary layer. This process is illustrated in Figure 2A. Under these conditions, the target concentration within the hydrogel quickly decays to zero, and the flux can be approximated by eq 2, where δ is the boundary layer thickness and $T_{s,0}$ is the target concentration at the edge of the hydrogel:

$$J \sim D_{gel}\frac{T_{s,0}}{\delta} \tag{2}$$

For reaction-diffusion mechanisms with high Da, the target never reaches the center of the particle and the boundary layer thickness is dependent on the relative rates of reaction and diffusion: $\delta \sim Da^{-1/2}L$.[44] Substituting this equation into eq 2, we obtain

$$J \sim D_{gel}^{1/2} k_a^{1/2} P_0^{1/2} T_{s,0} \tag{3}$$

At high Da, the flux into the particle is independent of the particle size. However, at low Da ($Da \ll 1$), the full hydrogel is utilized for the reaction and the concentration in the center of the hydrogel is nonzero, T_{center}, resulting in an estimated flux of

$$J \sim D_{gel}\frac{T_{s,0} - T_{center}}{L} \tag{4}$$

In a comparison of eq 2 and eq 4, the flux into a particle at high Da will always be higher than the flux into a particle at low Da since δ is less than L. To maximize hydrogel signal, then a higher Da is preferred.

So far we have concerned ourselves with 1D flux approximations, but ultimately, we are concerned with the amount of target bound at the end of the bioassay, as measured by the signal. Bioassays often use a fluorescent signal per unit imaging area as a quantification metric, taking a 2D image of the 3D particle, as shown in Figure 2B. Da values were calculated assuming a 10% incorporation of biotinylated probe into the hydrogel,[36] a forward rate constant of 10^5 M^{-1} s^{-1} (measured in the Supporting Information), a diffusivity of 5.66 × 10^{-11} m^2/s (previously measured in the hydrogels for a fluorescently labeled antibody[45]), and a radius of 100 μm. At high Da, the average signal is higher, but the capture is concentrated around the edges of the hydrogel particle, as is shown in Figure 2C.

Assuming a constant flux, and that the assay operates at high Da, the signal per unit imaging area can be calculated by multiplying the flux by the external surface area of the particle and the time, to obtain the total amount of target in the hydrogel:

$$\frac{\text{Signal}}{\text{Area}_{imaging}} \sim \frac{\text{Area}_{surface}}{\text{Area}_{imaging}} Jt = \frac{\text{Area}_{surface}}{\text{Area}_{imaging}} D_{gel}^{1/2} P_0^{1/2} k_a^{1/2} T_{s,0} t \tag{5}$$

To verify eq 5, we used cylindrical particles and varied the probe concentration from 5 to 500 nM in the hydrogel while keeping the shape of the hydrogel and the rest of the hydrogel composition constant. The resulting signal in the hydrogel particles is plotted against the square root of the probe concentration in Figure 3. Probe concentrations in the hydrogel were calculated by assuming a 10% incorporation rate from the monomer concentration.[36] The plot of signal versus $P_0^{1/2}$ is expected to be linear at Damköhler numbers >1, since eq 5 was developed by assuming the presence of a boundary layer in the flux calculation. At low Da, the flux is expected to decrease because of a nonzero target concentration in the center of the hydrogel, resulting in a lower measured signal than predicted by eq 5 and a deviation from linearity. However, we observe a linear signal decrease down to the lowest probe concentrations, equivalent to Da = 0.09, suggesting that at this Damköhler number the flux has not decreased substantially below the value predicted by eq 3.

DOI: 10.1021/acs.analchem.8b03728
Anal. Chem. 2018, 90, 13572−13579

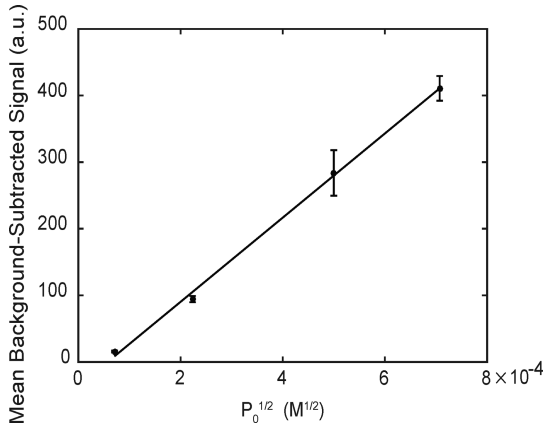

Figure 3. Mean background-subtracted signal increases with probe concentration in the hydrogel. The initial probe concentration was varied experimentally from 5 to 500 nM to change the flux into the particle. The line is a linear least-squares fit to the data. Each point is the mean of 3−4 particles and error bars represent standard deviations.

On the basis of eq 5, we can determine the parameters that influence the measured bioassay signal. Typically, the target concentration and the incubation time are set by required assay parameters, placing them outside of the researcher's control. To increase the signal, it is advantageous to increase the target diffusivity, the initial probe concentration, the reaction rate, and the ratio of the surface area to the imaging area. Depending on the specific target, k_a is usually set by the choice of target−probe pair, giving little control over that parameter. P_0 and D_{gel} can be influenced by manipulating the hydrogel prepolymer mixture, but often these are already optimized to a large extent during assay development. They are also sometimes coupled, making them difficult to control. For example, increasing the pore size of the hydrogel can result in higher diffusivity but lower probe incorporation.[36,46] As a result, changing the ratio of the surface area to the imaging area is the easiest way to influence assay signal. This parameter varies depending on the shape of the hydrogel. In a sphere, for example, the surface area is $4\pi R^2$ and the imaging area is πR^2, resulting in a ratio of surface area to imaging area that is independent of the size of the particle. However, with particles with more complex shapes such that the height is independent of the planar imaging area, there is an opportunity to tune the surface area to imaging area ratio to increase the signal. In a cylinder imaged through the planar surface as in Figure 2B, for example, the surface area to imaging area ratio is $\frac{2\pi R^2 + 2\pi RH}{\pi R^2} = 2\left(1 + \frac{H}{R}\right)$. We can therefore increase the signal by increasing the ratio of the height to the radius of the cylindrical particle (demonstrated in Figure S2 in the Supporting Information).

So far, we have considered nonoverlapping boundary layers in the theoretical analysis. As the hydrogel particle size is decreased, however, the boundary layers will come closer together, until they eventually overlap when the distance from the center of the particle to the edge is smaller than the boundary layer. It is of interest to know what happens to the flux during this scenario. To determine that, we must develop a model for the way the signal varies within the hydrogel. For simplicity, we begin with a 1D cylindrical system.

For the general case, the system can be described by species conservation equations, where $[T]$ is the target concentration, $[P]$ is the probe concentration, $[TP]$ is the concentration of the target−probe complex, t represents time, D_{gel} is the diffusivity of the target in the hydrogel, and k_a is the forward reaction rate. For a typical bioassay, the forward reaction rate is much faster than the reverse reaction rate (typical antibody K_D values are at least 10^{-7} s^{-1}),[47] so the reverse reaction is neglected for the model. In addition, typically, the probe concentration is in great excess of the target ($P_0 \sim 1$ μM, $T_{s,0} \sim 10^{-10}$ M), leading to a nearly constant probe concentration during the short assay time ($[P] \approx P_0$).

$$\frac{\partial [T]}{\partial t} = D_{gel}\nabla^2[T] - k_a[P][T] \tag{6}$$

This equation can be nondimensionalized by using $\hat{r} = \frac{r}{R}$, $\hat{T} = \frac{T}{T_{s,0}}$, and $\tau = \frac{t}{\frac{1}{k_a P_0}}$. For point-of-care bioassays, the target concentration is typically not significantly depleted during the assay, but the assay is longer than the characteristic reaction or diffusion time, leading to a pseudosteady target concentration within the hydrogel and resulting in the following non-dimensionalized equation, where $Da_R = \frac{k_a P_0 R^2}{D_{gel}}$:

$$0 = \frac{1}{\hat{r}}\frac{\partial}{\partial \hat{r}}\left(\hat{r}\frac{\partial \hat{T}}{\partial \hat{r}}\right) - Da_R\hat{T} \tag{7}$$

With this assumption, the 1D system can be solved for the target concentration as a function of position, using the boundary conditions

$$\hat{T}(\hat{r} = 1) = 1 \tag{8}$$

$$\frac{d\hat{T}}{d\hat{r}}(\hat{r} = 0) = 0 \tag{9}$$

The solution to these equations for the target concentration in the hydrogel uses modified Bessel functions:

$$\hat{T} = \frac{I_0(Da_R^{1/2}\hat{r})}{I_0(Da_R^{1/2})} \tag{10}$$

Ultimately, we are interested in the signal per unit imaging area, which we can calculate from the flux into the hydrogel. To find the flux into the radial face of the hydrogel, we can differentiate the dimensional version of eq 10 with respect to r, to calculate the 1D flux.

$$J = D_{gel}\frac{\partial T}{\partial r} = D_{gel}\frac{I_1\left(\frac{Da_R^{1/2}}{R}r\right)Da_R^{1/2}}{I_0(Da_R^{1/2})R}T_{s,0} \tag{11}$$

We evaluated the flux at the boundary where $r = R$ to calculate the expected signal per unit imaging area:

$$\frac{\text{Signal}}{\text{Area}_{\text{imaging}}} \sim \frac{2\pi RHtJ}{\pi R^2} = 2HtD_{gel}\frac{I_1(Da_R^{1/2})Da_R^{1/2}}{I_0(Da_R^{1/2})R^2}T_{s,0} \tag{12}$$

Equation 12 shows that as the radius decreases, the signal per unit imaging area increases, even in the case of overlapping boundary layers, although at very small values of Da_R, there is diminishing signal increase from further reduction of the radius. A plot of this equation can be viewed as Figure S3 in

DOI: 10.1021/acs.analchem.8b03728
Anal. Chem. 2018, 90, 13572−13579

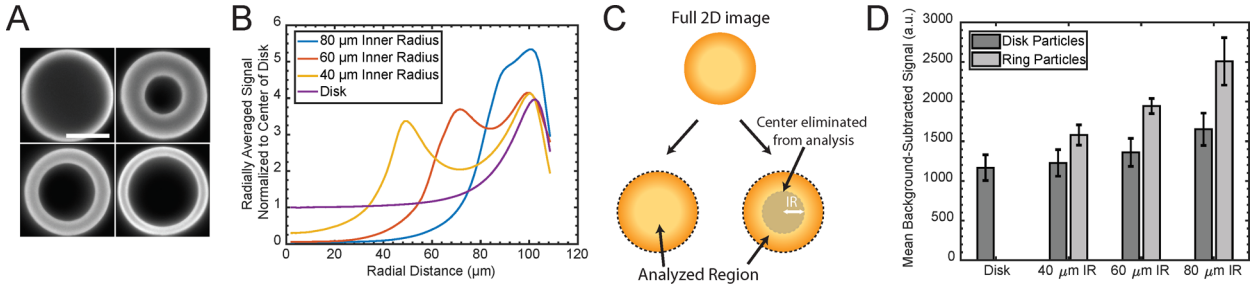

Figure 4. Adding internal boundary layers increases average signal within the hydrogels. (A) Fluorescent images of biotinylated hydrogel disk particles and rings with 40, 60, and 80 μm inner radii after reaction with 50 μg/L streptavidin−phycoerythrin. Scale bar is 100 μm. (B) Radially averaged signal in ring and disk particles, normalized to the signal in the center of the disk, plotted as a function of the radial distance. To obtain an accurate representation of the signal in the center, the signal in the inner 10 μm of the disk was averaged. Each line represents the average of five particles. (C) Analysis of disk particles. Either the full shape of the disk was analyzed or the analysis region was restricted to a ring shape of varying inner radius. (D) Comparison of signal between disk particles and ring particles. The disk particles were analyzed either by considering the full area or by eliminating a circle of the given inner radius in the center of the disk. Each bar represents five particles and error bars represent standard deviations.

the Supporting Information. The plot illustrates that this diminishing increase in signal occurs around $Da_R \sim 0.1$. We also verified that the trend of increasing signal with decreasing radius holds in the 3D case using COMSOL Multiphysics in the Supporting Information (Figure S3). To maximize the signal measured from a bioassay, it is therefore advantageous to decrease the cross-sectional area of the particle, down to at least $Da = 0.1$. We also verified this point experimentally by creating hydrogel posts with overlapping boundary layers (Figure S4). Because imaging particles with height larger than the diameter can prove challenging because of particle toppling, in the following sections we explore more complex shapes that reduce the imaging area of the particle while still maintaining a large outer radius.

Experimentally Manipulating Hydrogel Imaging Area. We sought to apply our knowledge of flux into the hydrogels to increase signal from a bioassay by decreasing the imaging area of hydrogel particles relative to the surface area. Technologies such as stop-flow lithography enable facile manipulation of particle shape and can provide a simple route to increase signal in POC bioassays. We began with cylindrical particles and increased fluorescent signal by adding internal features to create 3D extruded rings. This added an additional boundary layer on the inside of the ring, increasing the surface area to imaging area ratio. Images of these particles are shown in Figure 4A. These particles had a constant outer radius of 100 μm and an inner radius varying from 0 to 80 μm. To assess the relative fluorescence of each of the shapes, the radially averaged signal was plotted as a function of the radial distance (Figure 4B). To facilitate comparison, this signal was normalized to the inner signal in the disk particles and was plotted for the entire particle, including the region in the center of the rings. As the inner radius is increased, the boundary layers on the inner and outer ring surface begin to overlap, increasing the average signal within the particle. We then analyzed average signal within the particle. We predicted that some signal increase could be obtained by improved image processing through analyzing only the region on the edge of the disk particles since doing so increases the effective ratio of surface area to imaging area during the image analysis step. For example, for a cylinder imaged through one face, the ratio of the surface area to imaging area is $2\left(1 + \frac{H}{R}\right)$. By eliminating the center of the cylinder from the analysis and analyzing only a ring around the outside of the cylindrical particle, we found that the ratio increases to $2\left(1 + \frac{H}{R - \frac{2}{R}r_{inner}}\right)$, where R is the outer radius of the cylinder and r_{inner} is the radius of the inner circle eliminated from the analysis. By constructing particles of more complex shapes, such as 3D extruded rings, however, we can add an additional boundary layer around the inside of the ring, increasing the surface area to imaging area ratio to $2\left(1 + \frac{H}{R - r_{inner}}\right)$. The analysis method for the disk particles is shown in Figure 4C. The disks were analyzed both using the full area and by analyzing a ring-shaped region around the edges of the disk, neglecting the center. The results are plotted in Figure 4D, comparing the ring and disk shapes. Focusing the analysis on the outer regions of the disk-shaped particles results in a small improvement to the overall signal as the inner radius is increased from 0 μm (disk) to 80 μm. However, a much greater improvement in mean signal can be obtained by creating ring particles, adding an internal boundary layer. The rings with 80 μm inner radius show a more than twofold increase in mean signal above the signal in the disk particles. We observed occasional breakage of the 80 μm inner radius rings during the bioassay, so we did not fabricate rings with larger inner radii because of issues with structural integrity. However, we added additional inner features in the following section that could enable fabrication of thinner structures.

Application to Detection of TSH. We anticipated that increased signal in a bioassay would translate to reduced limit of detection (LOD), so we applied our strategy for increasing signal to POC detection of thyroid-stimulating hormone (TSH), an ~30 kDa serum protein. We used a sandwich assay format to detect TSH, capturing TSH from solution on immobilized capture antibodies within the hydrogel in the first step and labeling with a fluorescent detection antibody in the second step. Because the concentration of labeling protein can be increased during the assay to reduce incubation times, we focused on optimization of the target capture step. To do this, we created "wheel" particles with 20 μm feature thickness. We adopted the wheel motif because of observations that the rings with 80 μm inner radius often deformed during imaging or broke during the bioassay. By adding in the cross bars, we increased the rigidity of the particles.

DOI: 10.1021/acs.analchem.8b03728
Anal. Chem. 2018, 90, 13572−13579

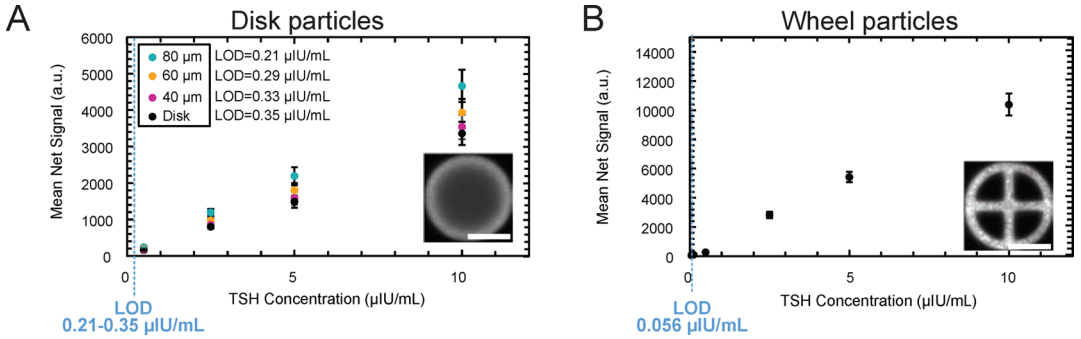

Figure 5. Calibration curves for detection of thyroid-stimulating hormone (TSH). (A) Calibration curve for disk particles. Each data point represents the average of three to five particles and error bars represent one standard deviation. Each disk was analyzed as the mean signal in either the full disk or in a ring-shaped region around the edge of the disk. Limit of detection (LOD) is calculated as the point where the signal is three standard deviations above the control. Inset figure is an image of a disk particle at 10 μIU/mL. Scale bar is 100 μm. (B) Calibration curve for wheel particles. Each data point represents the average mean signal of three to five particles and error bars represent one standard deviation. LOD represents point where signal is three standard deviations above control. Inset figure shows wheel particle after reaction with 10 μIU/mL TSH. Scale bar is 100 μm.

By using these wheel particles for detection of TSH, we both increased the fluorescent signal during the bioassay and decreased the limit of detection. Figure 5 shows calibration curves for the TSH assay. We constructed a calibration curve for TSH using disk particles (Figure 5A). The limit of detection was calculated as the point where the net signal was 3 times the noise (defined as the standard deviation of the control sample). The mean net signal refers to the difference between the background-subtracted signal and the background-subtracted signal of the control particles. We anticipated that some signal increase could be obtained by improved analysis methods and only utilizing the signal at the edges of the hydrogel for analysis. Reducing the analysis region to a ring with inner radius of 80 μm and outer radius of 100 μm improves the limit of detection slightly, from 0.35 to 0.21 μIU/mL. However, we anticipated that greater improvements in limit of detection could be achieved by adding internal surface area. For the "wheel" particles, the resulting limit of detection was 0.056 μIU/mL, a sixfold reduction in LOD (Figure 5B). In addition to improved signal in the wheel particles, we anticipate that the reduced diffusion length scale also improves washing in the particles, contributing to the LOD improvement. We observed that the standard deviation of the control particles was lower for the wheel particles than the disk particles by about a factor of 2, which we attribute to better washing. We also note that the signal in the particles has a splotchy appearance, which we attribute to antibody phase separation and can be improved by using monomer compositions with reduced PEG content (Figure S5).

CONCLUSIONS

We have developed a method of increasing signal for point-of-care bioassays by increasing the ratio of the surface area to the imaging area in hydrogel microparticles. By changing the particle shape, we added an additional boundary layer on the inside of the particle and increased the mean signal within the hydrogel. We derived equations to estimate the signal after a bioassay from the flux of target into the hydrogel that can provide guidelines for hydrogel shape design and we applied those guidelines to increase assay signal from a model biotin–streptavidin assay. Finally, we applied this technique to an assay for thyroid-stimulating hormone, resulting in a sixfold decrease in the assay limit of detection, simply through increasing the surface area relative to the imaging area. We anticipate that this strategy could be applied to many types of POC bioassays, enabling LOD reductions through changing particle shape, without needing to modify other assay parameters. This is particularly advantageous since often the researcher has limited control over the other parameters for POC bioassays.

ASSOCIATED CONTENT

Supporting Information

The Supporting Information is available free of charge on the ACS Publications website at DOI: 10.1021/acs.analchem.8b03728.

Calculations of forward rate constant, estimation of target depletion from solution, and COMSOL simulations and experiments of target captured in particles with overlapping boundary layers (PDF)

AUTHOR INFORMATION

Corresponding Author

*E-mail: pdoyle@mit.edu. Phone: (617) 253-4534.

ORCID

Sarah J. Shapiro: 0000-0003-2399-4928

Patrick S. Doyle: 0000-0003-2147-9172

Notes

The authors declare the following competing financial interest(s): D. Dendukuri is the CEO and co-founder and an employee of Achira Labs Pvt. Ltd. and P. Doyle is a scientific advisor to Achira Labs.

ACKNOWLEDGMENTS

The authors thank the Tata Center at MIT for funding. We also thank the Prather Lab at MIT for allowing us to use their NanoDrop for quantification of protein concentrations and L. Chen, M. Nagarajan, and A. Tentori at MIT for insightful discussions.

REFERENCES

(1) Le Goff, G. C.; Srinivas, R. L.; Hill, W. A.; Doyle, P. S. *Eur. Polym. J.* **2015**, *72*, 386–412.

(2) Aarstad, O.; Heggset, E. B.; Pedersen, I. S.; Bjørnøy, S. H.; Syverud, K.; Strand, B. L. *Polymers* **2017**, *9*, 378.

DOI: 10.1021/acs.analchem.8b03728
Anal. Chem. 2018, 90, 13572–13579

(3) Jamadi, M.; Shokrollahi, P.; Houshmand, B.; Joupari, M. D.; Mashhadiabbas, F.; Khademhosseini, A.; Annabi, N. *Macromol. Biosci.* **2017**, *17*, 1600479.
(4) Berger, J.; Reist, M.; Mayer, J. M.; Felt, O.; Peppas, N. A.; Gurny, R. *Eur. J. Pharm. Biopharm.* **2004**, *57*, 19−34.
(5) Fisher, S. A.; Baker, A. E.; Shoichet, M. S. *J. Am. Chem. Soc.* **2017**, *139*, 7416−7427.
(6) Pregibon, D. C.; Toner, M.; Doyle, P. S. *Science* **2007**, *315*, 1393−1396.
(7) Liu, E. Y.; Jung, S.; Yi, H. *Langmuir* **2016**, *32*, 11043−11054.
(8) Kim, J. J.; Bong, K. W.; Reátegui, E.; Irimia, D.; Doyle, P. S. *Nat. Mater.* **2017**, *16*, 139−146.
(9) Dendukuri, D.; Gu, S. S.; Pregibon, D. C.; Hatton, T. A.; Doyle, P. S. *Lab Chip* **2007**, *7*, 818−828.
(10) Yeh, J.; Ling, Y.; Karp, J. M.; Gantz, J.; Chandawarkar, A.; Eng, G.; Blumling, J., III; Langer, R.; Khademhosseini, A. *Biomaterials* **2006**, *27*, 5391−5398.
(11) He, Y.; Yang, F.; Zhao, H.; Gao, Q.; Xia, B.; Fu, J. *Sci. Rep.* **2016**, *6*, 29977.
(12) Wei, X.; Tian, T.; Jia, S.; Zhu, Z.; Ma, Y.; Sun, J.; Lin, Z.; Yang, C. J. *Anal. Chem.* **2016**, *88*, 2345−2352.
(13) Taylor, B. J.; Howell, A.; Martin, K. A.; Manage, D. P.; Gordy, W.; Campbell, S. D.; Lam, S.; Jin, A.; Polley, S. D.; Samuel, R. A.; et al. *Malar. J.* **2014**, *13*, 179.
(14) Yetisen, A. K.; Butt, H.; Volpatti, L. R.; Pavlichenko, I.; Humar, M.; Kwok, S. J. J.; Koo, H.; Kim, K. S.; Naydenova, I.; Khademhosseini, A.; et al. *Biotechnol. Adv.* **2016**, *34*, 250−271.
(15) Kost, G. J.; Tran, N. K.; Louie, R. F. *Encyclopedia of Analytical Chemistry*; American Cancer Society: 2008; pp 2−45.
(16) Larsson, A.; Greig-Pylypczuk, R.; Huisman, A. *Upsala J. Med. Sci.* **2015**, *120*, 1−10.
(17) Tsai, W. W.; Nash, D. B.; Seamonds, B.; Weir, G. J. *Clin. Ther.* **1994**, *16*, 898−910.
(18) Tayoun, A. N. A.; Burchard, P. R.; Malik, I.; Scherer, A.; Tsongalis, G. J. *Am. J. Clin. Pathol.* **2014**, *141*, 17−24.
(19) Peeling, R. W.; Mabey, D. *Clin. Microbiol. Infect.* **2010**, *16*, 1062−1069.
(20) Sohn, A. J.; Hickner, J. M.; Alem, F. *J. Am. Board Fam. Med.* **2016**, *29*, 371−376.
(21) Hortin, G. L.; Carr, S. A.; Anderson, N. L. *Clin. Chem.* **2010**, *56*, 149−151.
(22) Anderson, N. L.; Ptolemy, A. S.; Rifai, N. *Clin. Chem.* **2013**, *59*, 194−197.
(23) Lancet, T. *Lancet* **2012**, *379*, 1076.
(24) Szkudlinski, M. W.; Fremont, V.; Ronin, C.; Weintraub, B. D. *Physiol. Rev.* **2002**, *82*, 473−502.
(25) Ross, D. S. *Endocrinol. Metab. Clin. North Am.* **2001**, *30*, 245−264.
(26) Spencer, C. A. In *Endotext [Online]*; De Groot, L. J., Chrousos, G., Dungan, K., Feingold, K. R., Grossman, A., Hershman, J. M., Koch, C., Korbonits, M., McLachlan, R., New, M. et al., Eds.; MDText.com, Inc.: South Dartmouth, MA, 2000; http://www.ncbi.nlm.nih.gov/books/NBK279113/ (accessed May 11, 2018).
(27) Unnikrishnan, A. G.; Menon, U. V. *Indian J. Endocrinol. Metab.* **2011**, *15*, 78−81.
(28) Bagcchi, S. *Lancet Diabetes Endocrinol.* **2014**, *2*, 778.
(29) Unnikrishnan, A. G.; Kalra, S.; Sahay, R. K.; Bantwal, G.; John, M.; Tewari, N. *Indian J. Endocrinol. Metab.* **2013**, *17*, 647−652.
(30) Le Goff, G. C.; Lee, J.; Gupta, A.; Hill, W. A.; Doyle, P. S. *Adv. Sci.* **2015**, *2*, 1500149.
(31) Meiring, J. E.; Schmid, M. J.; Grayson, S. M.; Rathsack, B. M.; Johnson, D. M.; Kirby, R.; Kannappan, R.; Manthiram, K.; Hsia, B.; Hogan, Z. L.; et al. *Chem. Mater.* **2004**, *16*, 5574−5580.
(32) Kang, E.; Jung, S.; Abel, J. H.; Pine, A.; Yi, H. *Langmuir* **2016**, *32*, 5394−5402.
(33) Chen, L.; An, H. Z.; Haghgooie, R.; Shank, A. T.; Martel, J. M.; Toner, M.; Doyle, P. S. *Small* **2016**, *12*, 2001−2008.
(34) Kozlovskaya, V.; Alexander, J. F.; Wang, Y.; Kuncewicz, T.; Liu, X.; Godin, B.; Kharlampieva, E. *ACS Nano* **2014**, *8*, 5725−5737.
(35) Khademhosseini, A.; Langer, R. *Biomaterials* **2007**, *28*, 5087−5092.
(36) Pregibon, D. C.; Doyle, P. S. *Anal. Chem.* **2009**, *81*, 4873−4881.
(37) Zubtsov, D. A.; Savvateeva, E. N.; Rubina, A. Y.; Pan'kov, S. V.; Konovalova, E. V.; Moiseeva, O. V.; Chechetkin, V. R.; Zasedatelev, A. S. *Anal. Biochem.* **2007**, *368*, 205−213.
(38) Jokerst, J. V.; Chou, J.; Camp, J. P.; Wong, J.; Lennart, A.; Pollard, A. A.; Floriano, P. N.; Christodoulides, N.; Simmons, G. W.; Zhou, Y.; et al. *Small* **2011**, *7*, 613−624.
(39) Biondi, B.; Bartalena, L.; Cooper, D. S.; Hegedüs, L.; Laurberg, P.; Kahaly, G. J. *Eur. Thyroid J.* **2015**, *4*, 149−163.
(40) Spencer, C. A. *J. Clin. Immunoassay* **1989**, *12*, 82−89.
(41) Schneider, C. A.; Rasband, W. S.; Eliceiri, K. W. *Nat. Methods* **2012**, *9*, 671−675.
(42) Harris, J. M. Poly(Ethylene Glycol) Chemistry. *Topics in Applied Chemistry*; Springer: Boston, 1992; pp 1−14.
(43) Sharma, S.; Zapatero-Rodríguez, J.; Estrela, P.; O'Kennedy, R. *Biosensors* **2015**, *5*, 577−601.
(44) Deen, W. M. Analysis of transport phenomena. *Topics in chemical engineering*; Oxford University Press: New York, 2012; pp 5, 56.
(45) Appleyard, D. C.; Chapin, S. C.; Doyle, P. S. *Anal. Chem.* **2011**, *83*, 193−199.
(46) Choi, N. W.; Kim, J.; Chapin, S. C.; Duong, T.; Donohue, E.; Pandey, P.; Broom, W.; Hill, W. A.; Doyle, P. S. *Anal. Chem.* **2012**, *84*, 9370−9378.
(47) Zhang, H.; Williams, P. S.; Zborowski, M.; Chalmers, J. J. *Biotechnol. Bioeng.* **2006**, *95*, 812−829.

DOI: 10.1021/acs.analchem.8b03728
Anal. Chem. 2018, 90, 13572−13579